Abstract

Excessive warming is the source of many environmental challenges in urban areas. Finding causal interactions between urban ambient temperature and other meteorological variables will greatly facilitate our understanding of the underlying mechanisms of urban heat. In this study, we use the data of 2-meter air temperature and 500 hPa geopotential height (GPH) in 520 cities in the contiguous United States (CONUS), from 2016 to 2022, to detect their local and nonlocal causal interactions based on the convergent cross-mapping method. For local (within the same city) interactions between temperature and GPH, there are hubs of strong causal interactions in the northern Appalachian Mountain and inland southwestern CONUS, whereas the leeward side of the southern Rocky Mountains exhibit low causation due to the baroclinic in this area. The nonlocal causal networks exhibit potential long-range connections (teleconnections), largely attributable to the influence of the upstream and downstream westerly circulations on local atmospheric variables. This study can be informative to stakeholders in design sustainable countermeasures to mitigate excessive heat in urban areas.

Keywords: *Causality; Contiguous United States; Convergent cross mapping; Teleconnection; Urban microclimate*

1. Introduction

Urbanization has induced various challenges with complex human-environment interactions over built terrains. Examples include excessive heat, air pollution, and degradation of ecosystem services, to name a few, of which the phenomenon of urban heat island (UHI) is a prominent example (Oke, 1967, 1982). In addition, most cities in U.S. are experiencing a rising trend of heat extremes (often known as heatwaves or HWs) (Habeeb et al., 2015) as a consequence of global climate changes (IPCC, 2021), and the urban thermal environment is further exacerbated due to the synergistic interplay of UHI and HWs (Jiang et al., 2019). The efficacy of urban heat mitigation strategies therefore relies on our fundamental understanding of the intricate interactions of various meteorological and environmental variables underneath the phenomenon of elevated temperature, and their compound impact on urban environment (Wang, 2021). Up to date, tremendous research effort has been devoted to study the attribution of excessive urban heat to landscape characteristics, e.g., the coverage and distribution of urban vegetation, thermal properties of pavement materials (especially albedo), urban morphology, etc. that are *manageable* from the perspective of urban planners, practitioners, and policymakers (Hou et al., 2023a,b). In contrast, the contribution and attribution of background meteorological/climatic conditions to regulating the ambient temperature in cities remains relatively underexplored.

Among many meteorological conditions that affect urban thermal environment, atmospheric pressure systems play a critical role in regulating the thermal environment. In particular, “blocking” pressure systems strongly regulate the formation of heat and cold anomalies (HWs or cold spells) via their dynamic synchronization (Charney & Devore, 1979; Perkins, 2015; Chen & Luo, 2017; Wang et al., 2021). Meteorologically, the presence of

different pressure surfaces above mean sea-level is usually represented using the geopotential height (GPH). For example, GPH plays important roles in regulating the atmospheric circulation, including the distributions and movement of subtropical high, polar vortexes, ridges and troughs in the westerlies, etc. (Lu et al., 2008; Cao et al., 2020; Savelieva, 2020; Alizadeh & Lin, 2021; Tong et al., 2021), which, at the 500 hPa level, could influence the near-surface temperature dramatically (Yang et al., 2020).

Some research has been carried out to study the interactions between the near-surface temperature and GPH. It was found that GPH is regulated by surface temperature via the vertical profiles of air temperature and humidity (Wallace & Hobbs, 2006; Qin, 2009). On the other hand, the distribution of GPH is informative to the presence of ascending motions or descending motions and the directions of the air flow that in turn causes temperature anomalies (Rashid et al., 2020). The positive anomalies of GPH generally indicate the existence of high-pressure systems that lead to the sinking motions of the air parcel and thus increase the temperature of the middle and upper troposphere by adiabatic heating (Broccoli, 2012; Nath, 2012; El Kenawy et al., 2013; Olmo et al., 2020; Rashid et al., 2020). For example, the North Pacific Ocean subtropical high has been identified as a main cause of HWs in subtropical zones like south China, and the blocking high in the westerlies could trigger heatwave episodes in north China (Luo et al., 2020, 2022). On the contrary, the negative anomalies of GPH are often linked to abnormally low temperatures (El Kenawy et al., 2013).

To quantify the interactions between GPH and ambient temperatures, linear statistical correlation has been a prevailing technique adopted in the literature (Klein & Kline, 1984, 1986; Knapp & Yin, 1996). However, linear correlation analysis is prone to spurious couplings which are common in nonlinear systems, especially when two or more variables are driven by common

forcings (Pearl & Mackenzie, 2018). In contrast, causal inference methods, more sophisticated than statistical correlations, have been developed for nonlinear dynamic systems with coupled and interacting variables (e.g., the Earth's climate system), such as the Granger causality (GC) (Granger, 1969), convergent cross-mapping (CCM) (Sugihara et al., 2012), and partial cross mapping (Runge et al., 2015, 2019) methods. The GC method, however, often suffers from its applicability to purely stochastic and nonseparable systems as well as its stringent requirement of length of time series (Ancona, 2004; Sugihara et al., 2012).

The convergent and partial cross mapping methods, on the other hand, are particularly suitable for Earth systems (Sugihara et al., 2012; Runge, 2019). In particular, the CCM method has been lately applied to earth system sciences for detecting drivers and interactions among various variables of complex hydroclimate systems (Yang et al., 2022b, 2023a, b; Yu et al., 2022). Furthermore, the causal relationship among various environmental and meteorological variables in the built environment will facilitate the shift of paradigm from process-based to system-based urban environmental studies (Wang, 2022), which entails the use of rich set of advanced toolkits of data sciences and complex dynamic systems including, e.g. network analysis (Wang & Wang, 2020; Wang et al., 2020a), critical system transitions (Wang et al., 2020b; Yang et al., 2022a), and machine learning (Li et al., 2022, 2023; Hou et al., 2023b).

In this study, we adopt the CCM method (Sugihara et al., 2012), based on Taken's theory of delay-coordinate embedding (Takens, 1981), to quantify the interactions among urban temperature and other variables. Our study areas consist of a total number of 520 cities in the contiguous United States (CONUS), with long-term urban environmental monitoring from 2016 to 2022. In particular, we quantify both the local (intra-city) and nonlocal (inter-city) causal interactions of near-surface urban temperature and GPH. The findings of this study help to shed

new lights on the governing mechanisms underneath the excessive heat in urban areas, and will be informative to sustainable urban development in the long run.

2. Methods

2.1. Study areas and data processing

The research areas of this study consist of 520 urban areas with more than 50,000 population, retrieved from the Topologically Integrated Geographic Encoding and Referencing (TIGER) database, developed by U.S. Census Bureau (https://www.census.gov/geographies/mapping-files/time-series/geo/tiger-geodatabase-file.html). Each selected urban area contains a weather station located within (390) or adjacent to (130) the study areas, from the list of over 900 stations archived by the National Renewable Energy Laboratory's typical meteorological year (TMY3) database. **Figure 1** shows the map of all states, located in nine climate regions, in CONUS (**Fig. 1a**) and spatial distribution of urban fractions in our study areas of the selected 520 cities/towns (**Fig. 1b**). In addition, for each urban area, we retrieve the dataset for long-term monitoring of CONUS from the National Center for Atmospheric Research (NCAR) (https://rda.ucar.edu/datasets/ds083.3/). The data is on 0.25° by 0.25° grids with a time interval of 6 hours (00:00, 06:00, 12:00, and 18:00, UTC, every day). The variables we retrieved include 2-m air temperature, 500 hPa GPH, precipitation, volumetric soil moisture content (0-0.1m), and 2-m relative humidity from 01/01/2016 to 12/31/2022. The 6-hourly time series were first aggregated to yield 24-hour (diurnal) mean values.

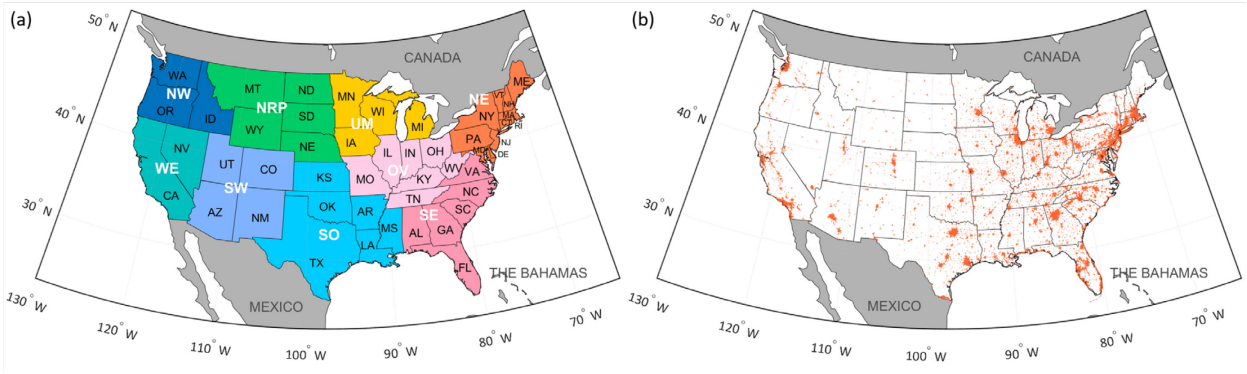

Figure 1. Spatial distributions of (a) the nine climate zones and all 48 states and (b) urban fractions of 520 urban areas in CONUS. The nine climate zones include Northwest (NW), North Rockies and Plains (NRP), West (WE), Southwest (SW), South (SO), Southeast (SE), Ohio Valley (OV), UM (Upper Middle), and NE (Northeast).

In addition, we obtained the anomalies of the "coarse-grained" daily time series, of GPH, temperature humidity, and soil moisture, by removing the daily means (averaged over all values of the same date within the study period). For precipitation, instead of anomalies, we calculated the Standardized Precipitation Index (SPI) of 30 days for each city, given by

$$\mathrm{SPI} = \frac{P - P^*}{\sigma_p}, \qquad (1)$$

where P is the accumulated precipitation of past 30 days, P^* is the 30-day average precipitation, σ_p is the standardized deviation of precipitation.

The anomalies and SPI are then used for subsequent causal analysis, as required by the input data format of the CCM algorithm. **Figure 2** shows the mean values of 500 hPa GPH and 2-m temperature of all the 520 cities averaged over the period of 01/01/2016 to 12/31/2022. The time series of daily anomalies of 500 hPa GPH and 2-m temperature are presented in **Fig. 3**, using Phoenix (33.43°N, 112.01°W) as an example.

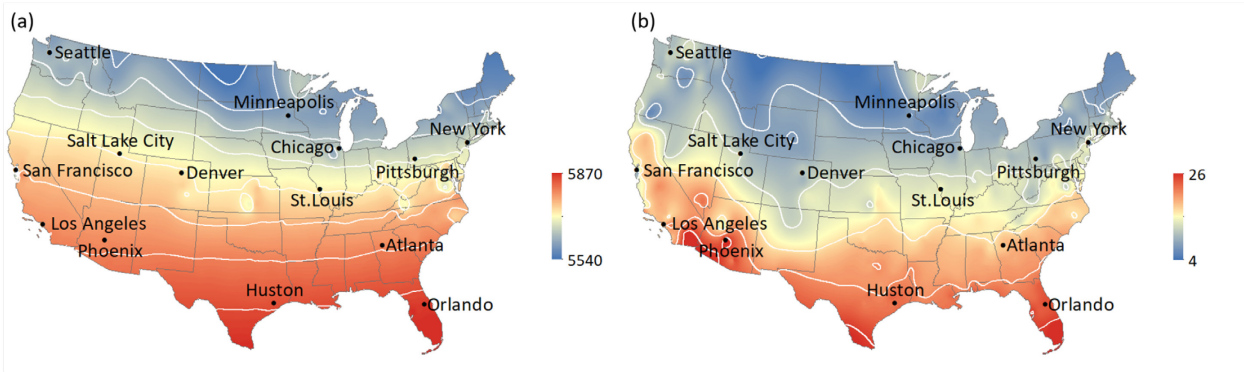

Figure 2. Sample plots of mean (a) The average 500 hPa GPH (gpm) and (b) 2-m temperature (°C) of the 520 CONUS cities averaged over 01/01/2016 to 12/31/2022.

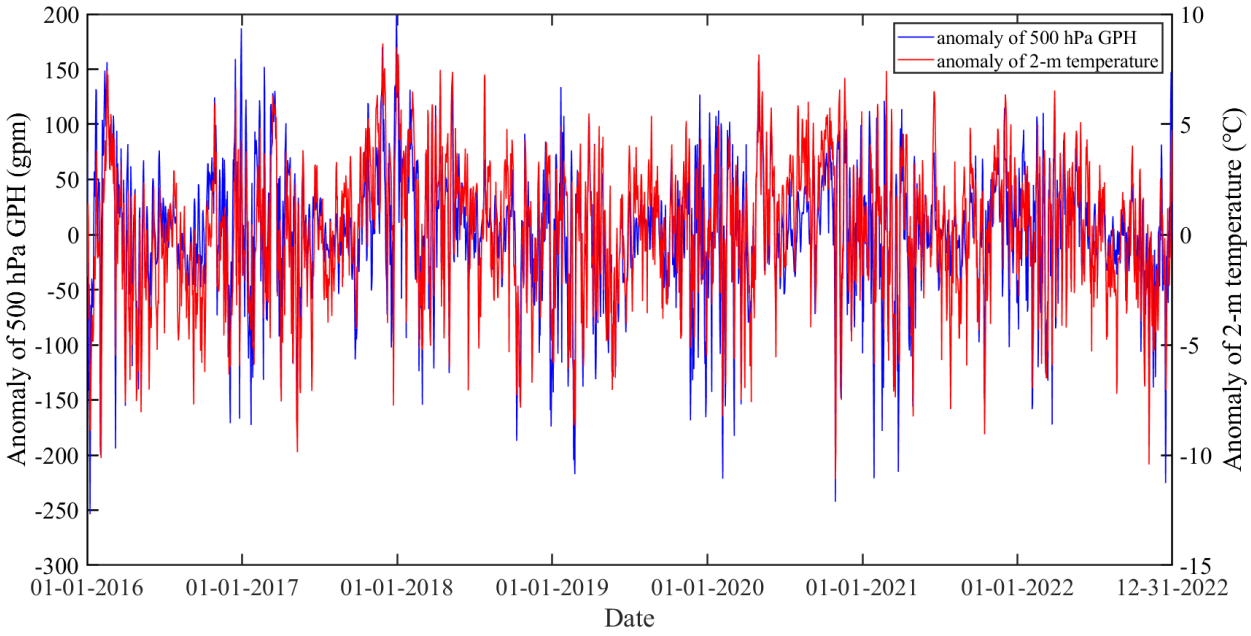

Figure 3. Sample time series of daily anomalies of 500 hPa GPH and 2-m temperature in Phoenix from 01/01/2016 to 12/31/2022.

2.2. The CCM method

The CCM method, based on the embedding theory (Takens, 1981), is designed to detect causality in deterministic nonlinear dynamic systems with weak to moderate couplings and

nonseparable variables (Sugihara et al., 2012). It adopts simple projection, which is a nearest-neighbor algorithm that uses the nearby points on the reconstructed manifolds to make kernel density estimations (Sugihara et al., 2012). Here we use the canonical Lorenz system, shown in **Fig. 4** with three dynamically coupled variables, X, Y, and Z, as an example of nonlinear dynamic systems to illustrate the CCM algorithm. To measure the causal effect between the time series of a pair of variables, e.g. $X(t)$ on $Y(t)$, we first build the shadow manifold M_X of th original time series $X(t)$, by constructing a lagged-coordinate vector given by $x(t) = [X(t), X(t-\tau), \ldots, X(t-(E-1)\tau)]$ (**Fig. 4b**), where τ is the time delay and E is the embedding dimension. Likewise, we can construct the shadow manifold M_Y. To determine the value of the time delay τ, we can use the value of the average oscillation period of $X(t)$. In addition, the correlation integral and dimension method can be used to determine the value of the embedding dimension E (see details in Jiang et al., 2016; Yang et al., 2022b). In this study, the values of $\tau = 1$ and $E = 3$ for subsequent analysis; the choice of these values are robust as proved by sensitivity test.

If there is causal coupling between the variables X and Y, there will be cross-mapping correspondence between their corresponding manifolds M_X and M_Y. For the time series $X(t)$, the cross-mapping estimate $\hat{X}(t) \mid M_Y$ is determined according to the projection of the $E+1$ nearest neighbors of vector $y(t)$ in the manifold of M_Y. The reason that $E+1$ points are requested is that $E+1$ is the minimum number of points needed for a bounded simplex in the E-dimensional space. Mathematically, time indices of the $E+1$ points on M_Y, $y(t_1), y(t_2), \ldots, y(t_{E+1})$, are used to identify the corresponding neighbors in X, i.e., $X(t_1), X(t_2), \ldots, X(t_{E+1})$, respectively. Thus, the cross-mapping estimate of $\hat{X}(t) \mid M_Y$ is calculated using the nearby $E+1$ points, as given by

$$\hat{X}(t) \mid M_Y = \sum_{i=1}^{E+1} w_i(t) X(t_i), \qquad (2)$$

where $w_i(t)$ are the weighting coefficients given by

$$w_i(t) = \frac{u_i(t)}{\sum_{j=1}^{E+1} u_i(t)}, \tag{3}$$

with

$$u_i(t) = \exp\left\{-\frac{d[y(t), y(t_i)]}{d[y(t), y(t_1)]}\right\}, \tag{4}$$

where $d[y(t), y(t_i)]$ is the Euclidean distance between $y(t)$ and $y(t_i)$ in M_Y.

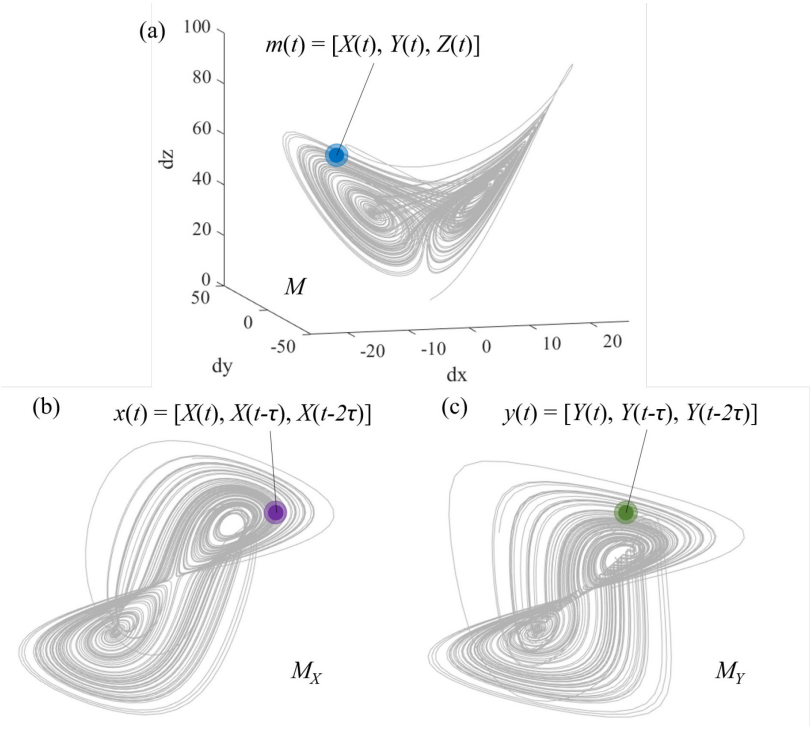

Figure 4. The illustration of the correspondence between two shadow manifolds of convergent cross mapping: (a) the canonical Lorenz system *m* consisting of three dynamically coupled variable *X*, *Y*, and *Z*, (b) the attractor projected onto the manifold of M_X, and (c) the attractor projected onto the manifold of M_Y.

Lastly, we calculate the correlation coefficient ρ between the estimated time series $\hat{X}(t) \mid M_Y$ and actual time series $X(t)$ to measure the causality from X to Y. More specifically, the correlation coefficient is defined as the CCM causality strength, denoted by $\rho_{X|M_Y}$ and is computed as

$$\rho_{X|M_Y} = \frac{\mathbf{E}\left\{\left[X(t) - \mu_X\right] \cdot \left[\hat{X}(t) \mid M_Y - \mu_{\hat{X}}\right]\right\}}{\sigma_X \sigma_{\hat{X}}}, \tag{5}$$

where $\mathbf{E}$, μ, and σ are the statistical expectation, average, and standard deviation, respectively. We can likewise define the causality $\rho_{Y|M_X}$ in the reverse direction (from Y to X). A higher value of ρ means a stronger causal relationship between a pair of variables.

Given the network of CONUS cities with N nodes (in our case $N = 520$), the computation of CCM strength will results in an $N \times N$ matrix $\rho(i, j)$ (the adjacency matrix, $i, j = 1, 2, 3 \ldots N$) for a given pair of variables X and Y, with the diagonal terms representing the local causality (time series X and Y are selected in the same city) and off-diagonal entities nonlocal causality. For the nonlocal causality, we further define average causal effect (ACE) and average causal susceptibility (ACS), by averaging over columns or rows of the adjacency matrix, respectively (Runge et al., 2015), as

$$\mathrm{ACE}_{X \to Y}(i) = \frac{1}{N-1} \sum_{j \neq i} \rho_{X|M_Y}(i, j), \tag{6}$$

$$\mathrm{ACS}_{X \to Y}(j) = \frac{1}{N-1} \sum_{i \neq j} \rho_{X|M_Y}(i, j). \tag{7}$$

Physically, ACE(i) can be interpretated as the mean capacity of an environmental variable X in a given city i to causally affect another variable Y averaged over the other N–1 cities, while ACS measures the susceptibility of that given city (to be causally influenced by other cities).

2.3. Selection of urban environmental variables

Out of the five urban environmental variables retrieved, viz. the 500 hPa GPH, 2-m temperature, 2-meter relative humidity, volumetric soil moisture content, and precipitation, we first prioritize the directional causal inference (effect and susceptibility) using the CCM method. The results of pair-wise average strength (over all study areas) of the CCM causality are shown in **Fig. 5**. It is clear that the pair of 500 hPa GPH and 2-m temperature stands out to have strongest *bi-directional* causal inference (with average strength greater than 0.4). The causal influence of precipitation on soil moisture manifested as the third highest, with apparent physical meaning, whereas the reserve causation (causal influence of soil moisture on precipitation, or causal susceptibility of precipitation to soil moisture) is insignificant. In the light of this test, we will focus on the causal inference between GPH and air temperature in the subsequent analysis.

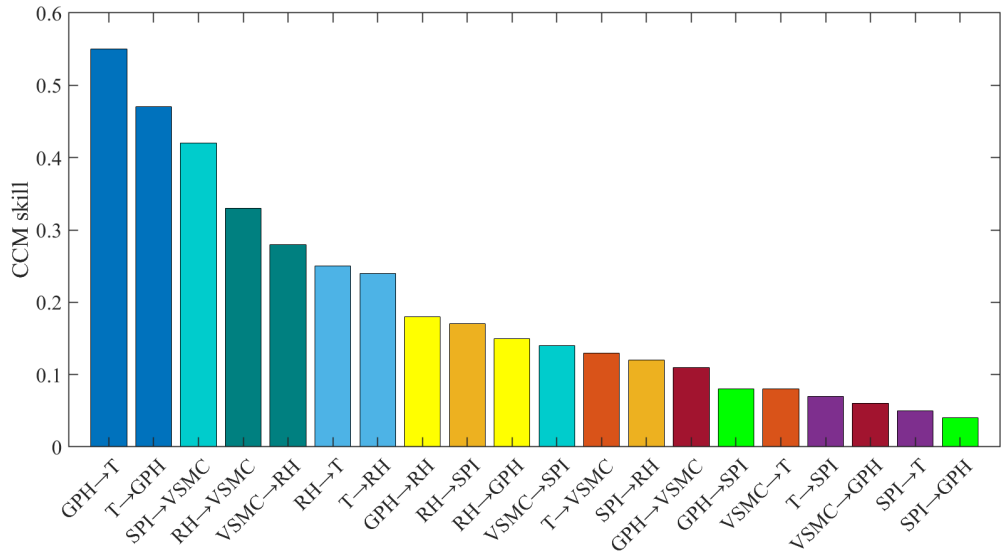

Figure 5. The average local CCM causality of the 520 cities between pairs of 5 variables. One pair in two directions are in the same color. GPH is 500 hPa geopotential height, T is 2-m temperature, SPI is the standardized precipitation index of 30 days, RH is 2-meter relative humidity, VSMC is volumetric soil moisture content.

3. Results and Discussion

3.1. The local temperature-GPH interactions

It is expected that GPH has a direct causal influence on local ambient temperature in a city before it can exert any potential long-range (trans-urban) impact on other cities. So, we first look into the bi-directional local causality between 500 hPa GPH and 2-m temperature which is mathematically represented by the diagonal terms of the adjacency matrices of $\rho_{X|M_Y}$ and $\rho_{Y|M_X}$, where X and Y are GPH and ambient temperature, respectively. The results of local causality are shown in **Fig. 6**.

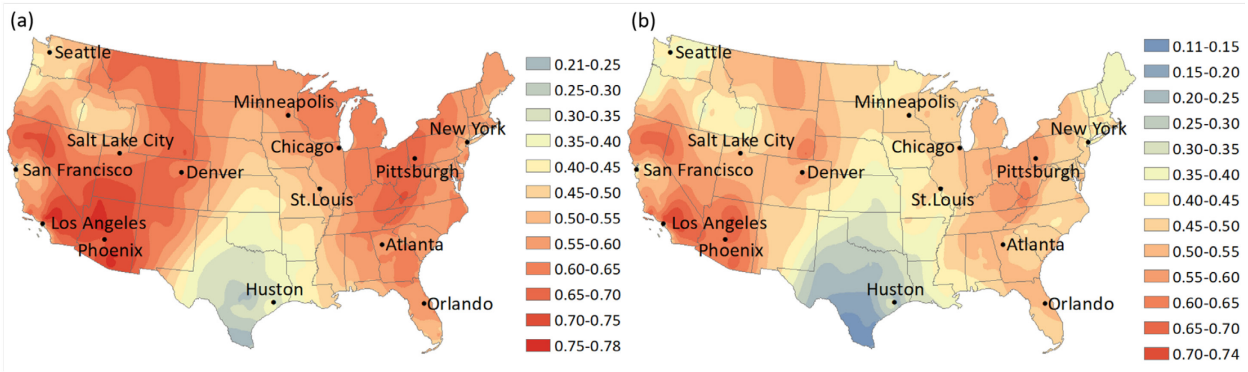

Figure 6. The distributions of the local directional causation between 2-m temperature and 500 hPa GPH: (a) from 500 hPa GPH to 2-m temperature, (b) from 2-m temperature to 500 hPa GPH.

First of all, it is noteworthy that, unlike the symmetrical linear statistical correlation, the CCM generated causation is asymmetrical. In general, the causal influence from 500 hPa GPH to 2-m temperature is stronger than the opposite direction for most of the CONUS cities, as shown in **Fig. 6**, indicating that atmospheric pressure strongly regulates the evolution of the thermal environment in cities. The spatial distribution of causation in CONUS cities, nevertheless, exhibits similar patterns in both directions, with two hubs of strong causations (ρ greater than

0.60) in the north Appalachian area (eastern half of OV climate zone) and southwest (i.e., Arizona (AZ) and inland southern California (CA)), respectively. In contrast, the southern leeward areas of the Rocky Mountains, i.e., Texas (TX) and its surrounding areas is manifested as a hub with weakest causal inference between GPH and temperature in CONUS. In addition, the NW climate region (Washington (WA) and southern Idaho (ID)) also appears as a local "weak" area, surrounded by strong causal influence zones.

The underlying mechanism of the spatial distributions of the local causation between GPH and temperature in CONUS is potentially governed by the lower atmosphere. It has been found that areas with less fog and clear sky tend to have strong coupling between the 500 hPa GPH and 2-m temperature (Kline & Klein, 1986; Knapp & Yin, 1996), which is likely responsible for the strong causal hubs in Arizona (AZ) and the inland areas of Southern California (CA). On the other hand, the GPH-temperature interactions can be decoupled due to atmospheric baroclinicity on the leeward areas of the Rocky Mountains (Klein & Kline, 1984) or the prevalence of heavy fog along the northwest coast (Kline & Klein, 1986). Such decoupling mechanisms, in turn, lead to the reduction of causal interactions between GPH and ambient temperature in these regions.

3.2. The nonlocal temperature-GPH interactions and potential teleconnection

We then look into the nonlocal causal interactions between GPH and temperature in CONUS cities, to identify, e.g., potential long-range connectivity (teleconnection) among CONUS cities, measured by ACE and ACS in Eqs. (6) and (7), respectively. The spatial distributions of ACE and ACS between 500hPa GPH and 2-m air temperature in CONUS cities are shown in **Figs. 7 and 8**. Overall, the nonlocal GPH-temperature causal interactions are much weaker than the local interactions, as expected. More specifically, **Fig. 7** shows that Ohio (OH),

Pennsylvania (PA) and the surrounding areas have the strongest nonlocal causal interactions from GPH to ambient temperature, followed by the inland Rocky Mountains area (SW climate zone, southwestern NRP climate zone, and inland NW and WE climate zone). The presence of these nonlocal causal hubs signals that, on average, atmospheric pressure systems (GPH) in cities of these areas exert stronger causal influence on (**Fig. 7a**), and are meanwhile more susceptible to (**Fig. 7b**), changes of thermal environment (temperature) in cities of *other* regions. In comparison, weak nonlocal interactions exist in the eastern leeward areas of the Rocky Mountains (eastern half of NRP climate zone and SO climate zone).

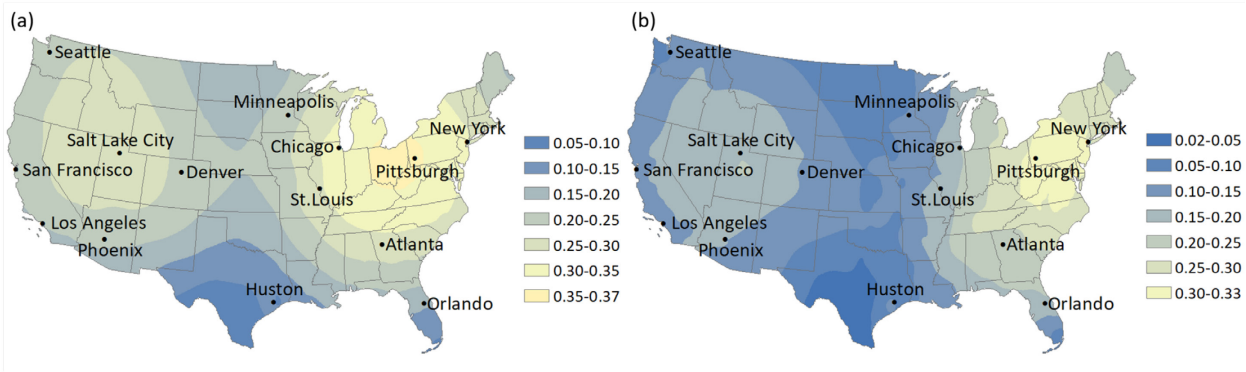

Figure 7. The distribution of the nonlocal causal interactions from 500 hPa GPH to 2-m air temperature in CONUS cities: (a) ACE and (b) ACS.

The spatial distribution of ACE and ACS from 2-m temperature to 500 hPa GPH, as shown in **Fig. 8**, exhibits two hubs of strong nonlocal causations and one hub of weak nonlocal causations all shifted southwestward, as compared to their counterparts in **Fig. 7**. In particular, a strong nonlocal causal hub is manifest to the east of the Mississippi River (eastern half of SO climate zone, OV climate zone, and SE climate zone), especially the areas surrounding Tennessee (TN). These hubs largely coincide with the presence of atmospheric gateways in Ohio

Valley (OV climate zone) for trans-regional transport of heat and precipitation, based on the causal analysis of long-term temperature and precipitation climatology in CONUS using the same CCM method (Yang et al., 2022b, 2023a). In addition, the presence of the causal hubs coincides well with "hot nodes" detected by machine-learning-based graphic neural network analysis that require most computational skills (Li et al., 2023), regardless the spatial resolution or regional aggregation of CONUS states.

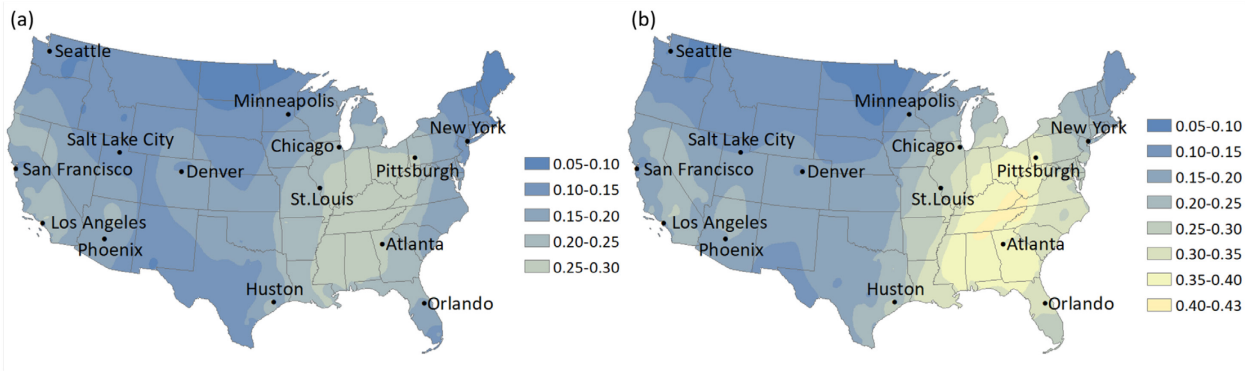

Figure 8. The distribution of the nonlocal causal interactions from 2-m air temperature to 500 hPa GPH in CONUS cities: (a) ACE and (b) ACS.

Furthermore, the spatial distribution of trans-urban interactions highlights the critical role played by the Rocky Mountains in modifying atmospheric circulations in CONUS. Located at mid-latitudes, the Rocky Mountains divide the westerly into two branches, making the airflow deflected and thus forming a ridge in the Rocky Mountains area and a trough in the downstream area of it, i.e., the Pacific-North American teleconnection pattern; the influence is more prominent in winter (Boyer & Chen, 1987; Xia et al., 2019; Wallace & Gutzler, 1981; Brayshaw et al., 2009). In addition, the Rocky Mountains can block the eastward movement of weather systems in the westerly (Spensberger et al., 2017). These orographically effects split the CONUS atmospheric circulations into two relatively independent subsystems, which has been

corroborated by recent studies of CONUS urban climate as complex dynamic systems. For example, it was found that the topology of CONUS urban climate networks has two manifest sub-clusters, separately located in the east and west CONUS (Wang & Wang, 2020; Wang et al., 2021), largely overlapped with the east (areas to the east of the Mississippi River) and west (the Rocky Mountains areas) hubs of nonlocal causal pressure-temperature interactions.

The nonlocal causal interactions in a given city measured by ACE and ACS are averaged over all *other* cities. Thus, the high-value hubs in **Figs. 7 and 8** may be resulted from strong trans-urban interactions among *adjacent* cities, but not necessarily indicate long-range (trans-regional) causal connection, despite that our previous work suggested the existence of teleconnection (Wang & Wang, 2020; Yang et al., 2022b, 2023a, b). To unravel the potential teleconnection of temperature-pressure interactions, we further look into causal connectivity of individual cities to all other cities (without averaging). **Figure 9** shows the causal susceptibility between 2-m temperature and 500 hPa GPH in four selected cities, viz. Chicago, New York, Orlando, and San Francisco in the CONUS. The contour plots clearly show that the causal susceptibility of an individual cities is indeed mostly contributed by surrounding urban areas, with the typical size of a central influence region (as indicated by the bright-colored region centering the selected city) covering a few adjacent states. Typically, the causal influence decays with distance.

Nevertheless, teleconnection across different climate regions does emerge in the mapping of causal susceptibility of thermal environment (2-m air temperature) in Orlando by pressure systems (500 hPa GPH) in other regions (**Fig. 9c**), as a second (slightly weaker) causal hub around the Salt Lake City. The presence of teleconnection can be physically attributed to the influence of the upstream and downstream westerly circulations on the local meteorological

variables of a city. For example, when the ridge or Alaska blocking high-pressure forms in the upstream areas of the CONUS, it will cause the downstream trough to deepen and further downstream ridge to occur, thereby facilitating the southward movement of cold air from Canada and causing negative temperature anomalies in the CONUS (Kline & Klein, 1986; Carrera et al., 2004). In addition, when the Greenland blocking high downstream of CONUS moves westward, it can also cause abnormal atmospheric circulation patterns and lower anomalies of temperature in the CONUS (Kline & Klein, 1986; Chen & Luo, 2017). Therefore, the centers of teleconnection could appear both in the upstream and downstream areas in the westerlies.

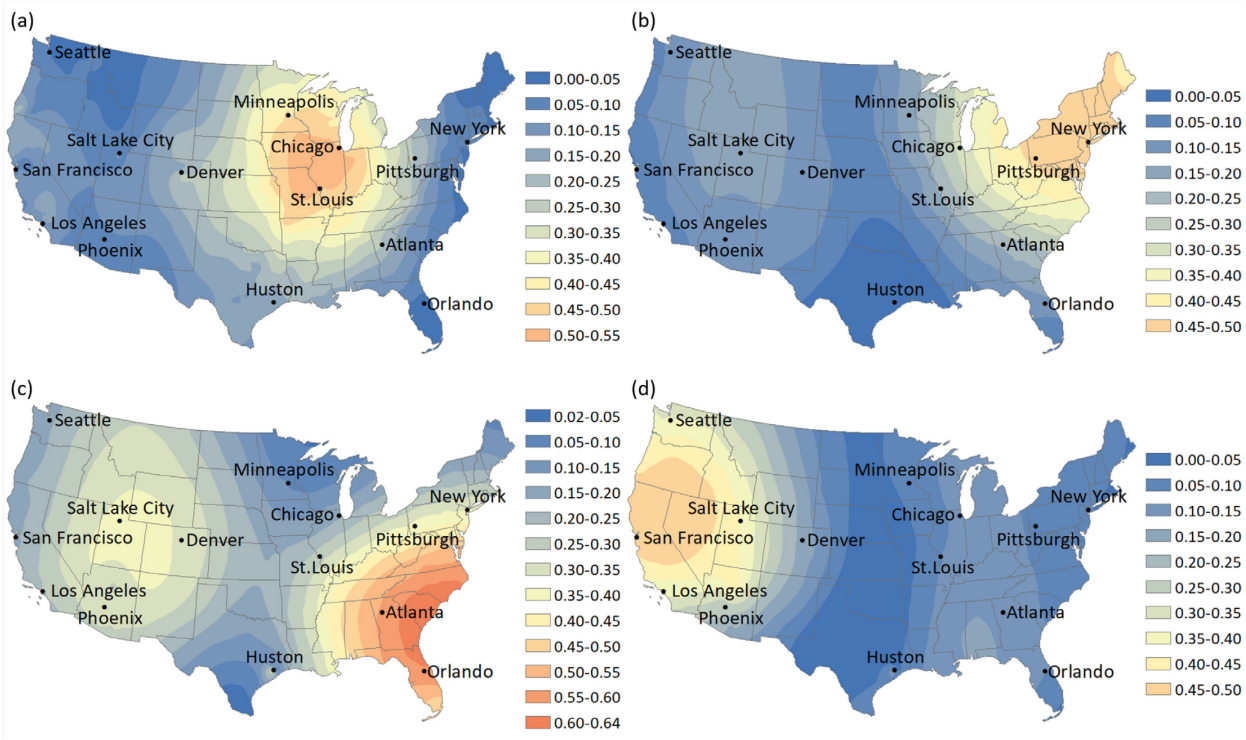

Figure 9. The causal susceptibility from 2-m temperature to 500 hPa GPH in (a) Chicago, and the causal susceptibility from 500 hPa GPH to 2-m temperature in (b) New York, (c) Orlando, and (d) San Francisco.

3.3. Implications to sustainable urban development

The exacerbated thermal environment in urban areas in the face of global climate change, excessive heat (e.g. the UHI effect) in particular, has been persistently challenging researchers and urban planners to seek sustainable solutions. In this study, we unravel the causal interactions of urban ambient temperature with distribution of pressure systems using the CCM method. In particular, it is found that the 2-m air temperature in a city is strongly regulated by the 500 hPa GPH presented in the locality, which in turn is influenced by the local urban thermal environment, resulting in effective two-way causal interactions.

Unlike urban landscape properties (e.g., albedo, pavement materials, urban infrastructure, building morphology, etc.), the presence of GPH *per se* is hardly manageable from the urban planning perspective. Nevertheless, its strong and two-way causal interactions with the ambient temperature suggest that sustainable urban strategies may be capable of inducing positive temperature-pressure feedback loop to facilitate the efficacy of heat mitigation. In particular, the identified hubs of strong causal interactions in CONUS implies that these are the core regions where the implementation of sustainable urban planning strategies are likely to be more effective and/or the efficacy of heat mitigation strategies can be extended to adjacent urban areas (periphery) that are causally influenced by these hubs. This is informative to policy makers as causal hubs are likely the areas worthy of more investment to promote the efficiency and sustainability of urban planning strategies. This implication, in the new light shed by the results of the current study, is far-reaching and certainly worth pursuing in future urban environmental research as to unraveling underlying mechanistic pathways governing the intricate interplay of various environmental/meteorological variables in the complex urban dynamic systems.

In addition, the presence of teleconnections in the nonlocal causal interactions, especially the susceptibility of urban temperature to long-range influence of dominating atmospheric pressure systems (such as blocking highs or lows), highlights the importance of coordinating the design, implementation, and evaluation of urban planning strategy adopted by different cities within or beyond their climate regions. Such synergy calls for the *network* approach inclusive of all relevant players, instead of isolated practices and/or policy making processes limited to the locality. Megacities and regional metropolitans are likely to weigh in more heavily in the cooperative processes not only because of their sizes and number of stakeholders, but also because they are more likely hubs of regional urban clustering than small or mid-sized towns in determining the topology of urban networks (Wang & Wang, 2020; Wang et al., 2020a).

4. Concluding Remarks

In this study, we use the CCM method to detect the causal interactions between 500 hPa GPH and 2-m temperature in the network of 520 U.S. cities. We identify the hubs of local and nonlocal causal interactions in CONUS, and the trans-regional teleconnections due to the westerly circulations. The results help to further our understanding of the mechanism of pressure distribution in causally mediating the thermal environment in cities and the potential temperature-pressure feedback due to their causal interactions. Nevertheless, there are other meteorological/environmental variables that can potentially regulate ambient temperatures in cities (e.g., radiation, cloud cover, anthropogenic emissions, etc.). This is particularly important in regions where temperature-pressure interactions are weak and supplementary forcings need to be included that can impact the thermal environment via local or long-range interactions.

While the current method can be readily extended to include other environmental variables, it is caveated that the causal interactions among multiple variables can be extremely complicated (recall one pair of variables generates four asymmetrical and directional complex causal graphs). In addition, the pair-wise causal relationship between two time series using CCM method also leaves the potential confounding effect among multiple factors rather elusive. Thus the key is to devise a novel protocol that can systematically process and evaluate the big amount of data to unravel the meaningful underlying causal mechanisms that govern the dynamic evolution of urban thermal environment. Recent advances in data science and dynamic systems offer a rich toolkit and promising perspective for developing such a novel protocol, by employing techniques such as network analysis, critical transitions and early-warning signals in urban climate system, and advanced machine learning algorithms (Wang, 2022). The system-based urban-climate modeling, with urban heat as a key component, also facilitate to find efficient strategies to counteract compound urban environmental impact through, e.g., multi-objective optimization (Li et al., 2022) and foster policy making processes.

Acknowledgement

This study is supported by the U. S. National Science Foundation (NSF) under Grant No. CBET-2028868 and AGS-2300548, and the National Aeronautics and Space Administration (NASA) under grant # 80NSSC20K1263.

References:

Alizadeh, O., and Lin, Z. (2021). Rapid Arctic warming and its link to the waviness and strength of the westerly jet stream over West Asia. *Global and Planetary Change*, 199, 103447.

Ancona, N., Marinazzo, D., and Stramaglia, S. (2004). Radial basis function approach to nonlinear Granger causality of time series. *Physical Review E*, 70(5), 056221.

Boyer, D.L., and Chen, R.R. (1987). Laboratory simulation of mountain effects on large-scale atmospheric motion systems: the Rocky Mountains. *Journal of Atmospheric Sciences*, 44(1), 100-123.

Brayshaw, D.J., Hoskins, B., and Blackburn, M. (2009). The basic ingredients of the North Atlantic storm track. Part I: land–sea contrast and orography. *Journal of the Atmospheric Sciences*, 66(9), 2539-2558.

Broccoli, A.J., and Loikith, P.C. (2012). Characteristics of observed atmospheric circulation patterns associated with temperature extremes over North America. *Journal of Climate*, 25(20), 7266-7281.

Cao, Y., Liang, S., and Yu, M. (2020). Observed low-frequency linkage between Northern Hemisphere tropical expansion and polar vortex weakening from 1979 to 2012. *Atmospheric Research*, 243, 105034.

Carrera, M.L., Higgins, R.W., and Kousky, V.E. (2004). Downstream weather impacts associated with atmospheric blocking over the northeast Pacific. *Journal of Climate*, 17(24), 4823-4839.

Charney, J.G., and Devore, J.G. (1979). Multiple flow equilibria in the atmosphere and blocking. *Journal of the Atmospheric Sciences*, 36(7), 1205-1216.

Chen, X., and Luo, D. (2017). Arctic sea ice decline and continental cold anomalies: upstream

and downstream effects of Greenland blocking. *Geophysical Research Letters*, 44(7), 3411-3419.

El Kenawy, A., López-Moreno, J.I., Brunsell, N.A., and Vicente-Serrano, S.M. (2013). Anomalously severe cold nights and warm days in northeastern Spain: their spatial variability, driving forces and future projections. *Global and Planetary Change*, 101, 12-32.

Granger, C.W. (1969). Investigating causal relations by econometric models and cross-spectral methods. *Econometrica: Journal of the Econometric Society*, 37(3), 424-438.

Habeeb, D., Vargo, J., and Stone, B. (2015). Rising heat wave trends in large US cities. *Natural Hazards*, 76(3), 1651-1665.

Hou, H., Su, H., Yao, C., & Wang, Z.H. (2023a), Spatiotemporal patterns of the impact of surface roughness and morphology on urban heat island, *Sustainable Cities and Society*, *92*, 104513.

Hou, H., Longyang, Q., Su, H., Zeng, R., Xu, T., and Wang, Z.H. (2023b). Prioritizing environmental determinants of urban heat islands: a machine learning study for major cities in China. *International Journal of Applied Earth Observation and Geoinformation*, 122, 103411.

IPCC. (2021). Weather and climate extreme events in a changing climate. *Climate Change 2021: The Physical Science Basis. Contribution of Working Group I to the Sixth Assessment Report of the Intergovernmental Panel on Climate Change*, Cambridge University Press, 1513-1766.

Jiang, J.J., Huang, Z.G., Huang, L., Liu, H., and Lai, Y.C. (2016). Directed dynamical influence is more detectable with noise. *Science Report*, 6(1), 24088.

Jiang, S.J., Lee, X., Wang, J.K., and Wang, K.C. (2019). Amplified urban heat islands during heat wave periods. *Journal of Geophysical Research-Atmospheres*, 124(14), 7797-7812.

Klein, W.H., and Kline, J.M. (1984). The synoptic climatology of monthly mean surface temperature in the United States during winter relative to the surrounding 700 mb height field. *Monthly Weather Review*, 112(3), 433-448.

Kline, J.M., and Klein, W.H. (1986). Synoptic climatology of monthly mean surface temperature in the United States during summer in relation to the surrounding 700-mb height field. *Monthly Weather Review*, 114(7), 1231-1250.

Knapp, P.A., and Yin, Z. (1996). Relationships between geopotential heights and temperature in the south-eastern US during wintertime warming and cooling periods. *International Journal of Climatology*, 16(2), 195-211.

Lai, Y.C., and Ye, N. (2003). Recent developments in chaotic time series analysis. *International Journal of Bifurcation and Chaos*, 13(6), 1383–1422.

Li, P., Xu, T., Wei, S., and Wang, Z.H. (2022). Multi-objective optimization of urban environmental system design using machine learning. *Computers, Environment and Urban Systems*, 94, 101796.

Li, P., Yu, Y., Huang, D., Wang, Z.H., and Sharma, A. (2023). Regional heatwave prediction using Graph Neural Network and weather station data. *Geophysical Research Letters*, 50, e2023GL103405.

Lu, R., Li, Y., and Ryu, C.S. (2008). Relationship between the zonal displacement of the western Pacific subtropical high and the dominant modes of low-tropospheric circulation in summer. *Progress in Natural Science*, 18(2), 161-165.

Luo, M., Ning, G., Xu, F., Wang, S., Liu, Z., and Yang, Y. (2020). Observed heatwave changes

in arid northwest China: physical mechanism and long-term trend. *Atmospheric Research*, 242, 105009.

Luo, M., Lau, N.C., and Liu, Z. (2022). Different mechanisms for daytime, nighttime, and compound heatwaves in southern China. *Weather and Climate Extremes*, 36, 100449.

Nath, M.J., and Lau, N.C. (2012). A model study of heat waves over North America: meteorological aspects and projections for the twenty-first century. *Journal of Climate*, 25(14), 4761-4784.

Oke, T.R. (1967). City size and the urban heat island. *Atmospheric Environment*, 7, 769-779.

Oke, T.R. (1982). The energetic basis of the urban heat island. *Quarterly Journal of the Royal Meteorological Society*, 108(455), 1-24.

Olmo, M., Bettolli, M.L., and Rusticucci, M. (2020). Atmospheric circulation influence on temperature and precipitation individual and compound daily extreme events: Spatial variability and trends over southern South America. *Weather and Climate Extremes*, 29, 100267.

Pearl, J., and Mackenzie, D. (2018). *The book of why: The new science of cause and effect*, Basic Books.

Perkins, S.E. (2015). A review on the scientific understanding of heatwaves-their measurement, driving mechanisms, and changes at the global scale. *Atmospheric Research*, 164, 242-267.

Qin, H., and Kawamura, H. (2009). Atmospheric response to a hot SST event in November 2006 as observed by the AIRS instrument. *Advances in Space Research*, 44(3), 395-400.

Rashid, I.U., Almazroui, M., Saeed, S., and Atif, R.M. (2020). Analysis of extreme summer temperatures in Saudi Arabia and the association with large-scale atmospheric circulation. *Atmospheric Research*, 231, 104659.

Runge, J., Petoukhov, V., Donges, J.F., Hlinka, J., Jajcay, N., Vejmelka, M., et al. (2015). Identifying causal gateways and mediators in complex spatio-temporal systems. *Nature Communications*, 6, 8502.

Runge, J., Bathiany, S., Bollt, E., Camps-Valls, G., Coumou, D., Deyle, E., et al. (2019). Inferring causation from time series in Earth system sciences. *Nature Communications*, 10, 2553.

Savelieva, E. (2020). Possible influence of the tropospheric polar vortex on the Barents Sea ice extent in winter. *Journal of Atmospheric and Solar-Terrestrial Physics*, 197, 105173.

Spensberger, C., Egger, J., and Spengler, T. (2017). Synoptic systems interacting with the Rocky Mountain barrier: observations and theories. *Monthly Weather Review*, 145(3), 783-794.

Sugihara, G., May, R., Ye, H., Hsieh, C.H., Deyle, E., Fogarty, M., and Munch, S. (2012). Detecting causality in complex ecosystems. *Science*, 338(6106), 496-500.

Takens, F. (1981). Detecting strange attractors in fluid turbulence. *Dynamical Systems and Turbulence, Warwick 1980: proceedings of a symposium held at the University of Warwick 1979/80*, Springer Berlin Heidelberg, 366-381.

Tong, Q., Huang, Y., Duan, M., and Zhao, Q. (2021). Possible contribution of the PDO to the eastward retreat of the western pacific subtropical high. *Atmospheric and Oceanic Science Letters*, 14(1), 100005.

Wallace, J.M., and Gutzler, D.S. (1981). Teleconnections in the geopotential height field during the northern hemisphere winter. *Monthly Weather Review*, 109(4), 784-812.

Wallace, J., and Hobbs, P. (2006). *Atmospheric Science: An Introductory Survey* (second edition). Elsevier Academic Press.

Wang, C., and Wang, Z.H. (2020). A network-based toolkit for evaluation and intercomparison

of weather prediction and climate modeling. *Journal of Environmental Management*, 268, 110709.

Wang, C., Wang, Z.H., and Li, Q. (2020a). Emergence of urban clustering among U.S. cities under environmental stressors. *Sustainable Cities and Society*, 63, 102481.

Wang, C., Wang, Z.H., and Sun, L. (2020b). Early warning signals for critical temperature transition. *Geophysical Research Letters*, 47, e2020GL088503.

Wang, Z.H. (2021). Compound environmental impact of urban mitigation strategies: co-benefits, trade-offs, and unintended consequence. *Sustainable Cities and Society*, 75, 103284.

Wang, Z.H. (2022). Reconceptualizing urban heat island: beyond the urban-rural dichotomy. *Sustainable Cities and Society*, 77, 103581.

Wang, Z.H., Wang, C., and Yang, X. (2021). Dynamic synchronization of extreme heat in complex climate networks in the contiguous United States. *Urban Climate*, 38, 100909.

Xia, X., Ren, R., and Yu, Y. (2019). Dynamical role of the Rocky Mountain controlled by East Asian topographies in modulating the tropospheric westerly jet in northern winter. *Atmospheric and Oceanic Science Letters*, 12(1), 66-72.

Yang, S., Wang, L., Stathopoulos, T., and Marey, A.M. (2023). Urban microclimate and its impact on built environment – a review. *Building and Environment*, 238, 110334.

Yang, X., Wang, Z.H., and Wang, C. (2022a). Critical transitions in the hydrological system: early-warning signals and network analysis. *Hydrology and Earth System Sciences*, 26(7), 1845-1856.

Yang, X., Wang, Z.H., Wang, C., and Lai, Y.C. (2022b). Detecting the causal influence of thermal environments among climate regions in the United States. *Journal of Environmental Management*, 322, 116001.

Yang, X., Wang, Z.H., Wang, C., and Lai, Y.C. (2023a). Finding causal gateways of precipitation over the contiguous United States. *Geophysical Research Letters*, 50(4), e2022GL101942.

Yang, X., Li, P., and Wang, Z.H. (2023b). The impact of urban irrigation on the temperature-carbon feedback in U.S. cities. *Journal of Environmental Management*, 344, 118452.

Yang, Y., Gao, M., Xie, N., and Gao, Z. (2020). Relating anomalous large-scale atmospheric circulation patterns to temperature and precipitation anomalies in the East Asian monsoon region. *Atmospheric Research*, 232, 104679.

Ye, H., Deyle, E.R., Gilarranz, L.J., and Sugihara, G. (2015). Distinguishing time-delayed causal interactions using convergent cross mapping. *Science Report*, 5, 14750.

Yu, Y., Shang, G., Duan, S., et al. (2022). Quantifying the influences of driving factors on land surface temperature during 2003–2018 in China using convergent cross mapping method. *Remote Sensing*, 14(14), 3280.

Zak, M., Nita, I.A., Dumitrescu, A., and Cheval, S. (2020). Influence of synoptic scale atmospheric circulation on the development of urban heat island in Prague and Bucharest. *Urban Climate*, 34, 100681.